Improvements in fast mass microscopy for large-area samples

Edith Sandström,[a] Pascal Huysmans,[b] Frans Giskes,[a] Paul Laeven,[b] Sebastiaan Van Nuffel,[a] Ron M. A. Heeren,[a] Ian G. M. Anthony[a*]

[a]The Maastricht MultiModal Molecular Imaging Institute (M4i), Division of Imaging Mass Spectrometry, Maastricht University, Maastricht 6229 ER, The Netherlands, [b]Instrument Development, Engineering & Evaluation (IDEE), Maastricht University, Maastricht 6229 ER, The Netherlands

Mass spectrometry imaging (MSI) is a technique that analyzes chemical information and spatial distribution of surface analytes. Most MSI studies are conducted in microprobe-mode, in which a mass spectrum is collected for each pixel to create a mass image. Thus, spatial resolution, sample imaging area, and imaging speed are linked. In this mode, halving the pixel size quadruples the analytical time, which presents a practical limit on high spatial resolution MSI throughput. Fast mass microscopy (FMM) is, in contrast, a microscope-mode MSI technique which decouples spatial resolution and imaging speed. FMM circumvents the linear-quadratic relationship of pixel size and analytical time which enables increased the imaging size area and the analytical speed achievable. In this study, we implement instrument modifications to the FMM system including the addition of linear encoders that enable roughly 8.5× faster imaging than was previously achieved, allowing a 42.5×26 mm^2 sample area to be imaged at a 1 μm pixel size in < 4.5 min. Linear encoders also enable the alignment of multi-pass images that increase image homogeneity and chemical signal. The applicability of FMM to large area samples has made it important to define the tolerance to height variations of the technique, which was determined to be at least 218 μm.

Introduction

Mass spectrometry imaging (MSI) is an analytical technique that obtains chemical information along with its spatial distribution.[1,2] The ability of MSI to simultaneously image thousands of molecules in a single experiment makes it a powerful tool for fields varying from biomedical[3–5] and forensic[6,7] to material[8] and heritage[9–11] sciences. The most common mode of MSI is microprobe-mode, wherein a laser or ion beam is scanned serially over the sample collecting a mass spectrum per pixel.[12] Halving the pixel size in microprobe mode thus requires quadrupling the number of pixels and thus analysis time. This linear-quadratic relationship limits the size of the sample area that is practical to analyze by MSI in microprobe mode at high spatial resolutions.[13,14]

A strategy to circumvent this linear-quadratic relationship is microscope-mode MSI, also known as mass microscopy,[15] in which a defocused ion beam generates ions from the sample surface under high vacuum conditions. The relative spatial locations of the ions are preserved using stigmatic ion optics during time-of-flight (TOF) mass analysis. The mass and spatial information is then collected simultaneously by a pixelated TOF detector. An advantage of microscope-mode MSI is that the pixel size of images generated is independent of spatial resolving power and beam spot size.[16–20]

Fast mass microscopy (FMM) is a microscope-mode MSI technique that uses a fast-moving sample stage and a fast pixelated detector, such as a TPX3CAM, to allow investigation of larger areas at short timescales. In a previous study, FMM was used to image a 42×23.5 mm^2 area in 33.5 minutes at a pixel size of 0.9 μm.[21] This speed is orders of magnitude faster than microscope-mode MSI. Although fast, the previously reported FMM results were still limited in speed because they made use of interpolation of the sample stage location for positioning the ion images. Linear interpolation is inaccurate and imprecise at higher stage velocities. Furthermore, due to variations in motor acceleration and timing,

the estimation was also not reproducible at the 1 μm scale between replicate measurements.

Herein, we remove the need for interpolation using linear encoders that provide exact positions of the sample stage for each TOF cycle. We use the encoder-provided coordinates to successfully image a 42.5×26 mm^2 area in < 4.5 minutes at a pixel size of 1 μm, which corresponds to approximately an eightfold speed increase compared to the previously reported study. Using the precise positioning of the encoders, we demonstrate that multiple fast passes of a large area can be taken quickly and improved the quality of the image reconstruction. As a result, image homogeneity is improved, and a dynamic-time mode of imaging is enabled. Additionally, we investigate the limits of topographical differences of the FMM instrument as these are relevant for reliable imaging of large-area samples.

Materials and Methods

Instrumentation

The BioTRIFT system used includes a C$_{60}$ ion beam (IOGC60-20S, Ion-optika, Chandler's Ford, UK) and a Timepix3 ASIC-based camera (TPX3CAM, Amsterdam Scientific Instruments, Amsterdam, NL) and is described in detail elsewhere.[21] Two linear encoders (LS 477, Heidenhain, Traunreut, DE) connected to a digitization card (NI6612, National Instruments, Austin, TX, USA) were added to the BioTRIFT stage directly under the existing encoders, allowing both normal instrument operation (**Figure S1**). The addition of the new encoders allowed for the instrument stage control to continue to function normally and without any hardware or software modifications. A NI6612 digitization card was used in conjunction with the new encoders to save the X and Y coordinates of the stage for every TOF cycle. Software performing this synchronized collection was written in LabVIEW 2020 32-bit (National Instruments, Austin, TX, USA) as a custom program. These coordinates files were combined with the respective TPX3CAM ".tpx3" file in

postprocessing to produce the mass images. The postprocessing workflow is described previously[21] but has been modified to either use the coordinates from the encoder files or to use the interpolated stage position (e.g., if no encoder files were collected). The primary TOF trigger was split using a Standford Research Systems DG535 delay generator and the resulting split signals were supplied to the C_{60} ion gun pulser, the TPX3CAM detector TDC input, and the NI6612 digitization card.

A FIB-SEM (Scios 2 DualBeam system (Thermo Fisher Scientific, Waltham, MA, USA) was used to measure the height at points on each stacked grid relative to the ITO slide. The SEM micrograph of the stack of grids can be seen in **Figure S2**.

Mass Spectrometry imaging

The C_{60} ion beam aperture was set to 1 mm resulting in a field of view of approximately 320 μm in diameter, and a continuous ion beam current of 0.5–0.8 nA at a source temperature of 410 °C. The largest contrast diaphragm aperture of the BioTRIFT was used for all images.

Materials

A hexagonal 400 mesh thin bar Cu grid was imaged to compare images with and without the encoder data. Hexagonal 200 mesh Cu grids were used for the stack of grids. A hexagonal 460 mesh Cu grid and a bar 400 mesh Ni grid were added to the composed surface sample. All TEM grids were obtained from Agar Scientific, UK. Indium Tin Oxide (ITO) coated glass slides (Delta Technologies, Loveland, CO, USA) were used for all samples. $Gd(III)Cl_3·6H_2O$, $Ho(III)Cl_3·6H_2O$, and red phosphorus were purchased from Merck, Germany. The lemon and table salt (NaCl) were purchased locally.

Sample preparation

For comparison of image construction with and without encoder-supplied coordinates, an Indium Tin Oxide (ITO) coated glass slide was prepared with a TEM grid secured with ink from a highlighter marker. To determine focal depth tolerance, on a separate ITO slide, five TEM grids were stacked on top of each other. Each grid was adhered with a highlighter marker before the next was placed on top off-center to create a "staircase" shape approximately 200 μm in height measured from the surface of the ITO coated slide. To add additional stack height, the top grid was bent slightly before placement on the stack of grid to create a "ramp" in the z-direction of approximately 200–500 μm in height measured from the surface of the ITO coated slide.

For the "composed surface" dataset, a lemon purchased from a local supermarket was cut into wedges. The wedges were loosely wrapped in aluminum foil and placed in a container of dry ice for 1 hour to freeze. A Microm HM535 cryo-microtome (Microm International) at a temperature of -20°C was used to produce 50 μm thick sections. The sample was then thaw-mounted onto a clean ITO coated glass slide and immediately placed into a vacuum desiccator to dry for 30 minutes before storage at -80°C.

On the day of the measurement, a saturated aqueous solution of NaCl was prepared and the operator's thumb was immersed in the saturated NaCl solution before being pressed next to the lemon to produce a fingerprint. Two TEM grids were placed on the slide and then adhered by dabbing them with a highlighter marker. Approximately 100 μL of an aqueous $GdCl_3$ solution (10 mg mL^{-1}) and an aqueous $HoCl_3$ solution (10 mg mL^{-1}) were pipetted onto the slide. The slide was then allowed to dry for 1 h at room temperature and pressure, and finally ~70 mg of red phosphorus was sprinkled across the slide. The slide was then sputter

coated with a 1.1 μm Au layer (SC7640, originally Polaron Ltd, now Quorum Technologies, Laughton, UK) before the measurement. The intention behind this composed surface sample was to produce a large area "test" sample with distinct mass images and fine spatial features that were resolved in the mass domain and partially resolved in the spatial domain.

Measurement

All measurements presented used a m/z range of 0.5 – 200 Da. The singular TEM grid was imaged with settings of 350 shots per area, C_{60} pulse time of 300 ns, and row-overlap of 90%. The measurement of the stack of grids settings were 10 000 shots per area, C_{60} pulse time of 300 ns, and row-overlap of 75%. The composed sample was first imaged with 300 shots per area, a C_{60} pulse of 500 ns, and a row-overlap of 30%. The investigated area was 42.5 × 26 mm measured in 264.6 s. Six subsequent images of the composed sample surface were imaged with varying settings of pulse times of 150–500 ns, row-overlaps of 30–40%, and 300 shots per area.

Results and Discussion

Advantages of linear encoder coordinates

Linear encoders were installed beneath the original stage encoders of the fast mass microscope (Figure S1). Use of encoders is common in imaging and manufacturing positioning equipment because knowledge of the precise position is of importance.[22] Recently, their introduction with the microgrid technology (Bruker, Billerica, MA, USA) facilitates high quality < 5 μm spatial resolution MALDI-MSI analysis by enabling more accurate laser beam positioning.

The interpolation method of FMM image construction assumes constant stage and sample velocity. By knowing the length, start and end time of each row imaged, the position of the individual ion images can be estimated by linear interpolation. It was observed that image artifacts and errors increased with higher stage speeds as well as shorter row lengths. With the encoders, each TOF cycle has a corresponding set of coordinates that enable accurate positioning of ions at any achievable stage velocities — e.g., a maximum of 3.2 cm s^{-1} was recorded on the BioTRIFT instrument, but higher velocities should be possible.
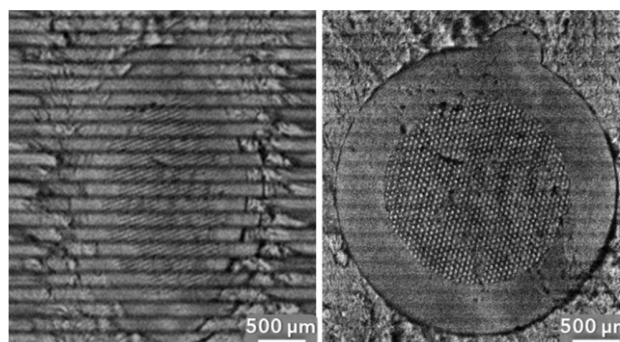
Figure 1. An FMM total ion count (TIC) image of a TEM grid constructed by the previous method of coordinate estimation by interpolation (**left**) and the use of the exact encoder coordinates (**right**). The same TPX3CAM data was used for both images.

The effect of the encoder coordinates on the total ion image was tested on a 4 × 4 mm area containing a TEM grid, imaged in 38 s at a speed of 0.42 mm^2 s^{-1} (420 000 pixel s^{-1} at 1 μm pixel size). The same TPX3CAM data was used for both images in **Figure 1**. The use of the interpolated coordinates (Figure 1, left) is clearly inferior and leads to row-mismatch,

blur, and image distortion when compared to the use of exact encoder coordinates (Figure 1, right).

The horizontal bands seen in both constructed images in Figure 1 can be reduced by optimizing the row overlap or by use of multiple imaging scans. However, at high speeds, alignment of multiple imaging scans is only feasible by the incorporation of the encoder coordinates, which makes the imaging measurement reproducible and more accurate.

Measurement of FMM focal depth

In microprobe mass spectrometry imaging, variation of surface height of even a few micrometers may cause changes in beam focus leading to loss of sensitivity.[23–25] This problem is severe enough that multiple microprobe systems incorporate autofocusing systems to enable imaging of uneven surfaces, often by incorporating a third axis into their imaging stages to enable compensating for surface height variation.[26–29] In a previous work, we noted that the use of an already defocused beam, such as that used in mass microscopy, reduces the negative effects of beam defocusing due to topographical differences across a sample.[21]

This tolerance to topographical height differences is of particular interest to large spatial area imaging applications because larger areas tend to have more surface height variations than local areas. In the authors' experience, MSI-prepared biological tissue samples are sectioned at thicknesses at or below 50 μm. Thus, a large-area imaging technique for biological tissues should ideally be robust over this height. The topographical tolerance of the FMM system was investigated on TEM grids stacked on top of each other with the top grid bent upwards, creating a surface with a height variation of at least 484 μm.

Figure 2 shows an FMM TIC image of the stack of TEM grids. Spots on the stack of grids were measured for their surface height using SEM. The total ion intensity and image sharpness appears no different between 0 to 218 μm of surface height. However, a decrease in signal intensity and increase in image blur can be observed at 484 μm, highlighted in a brightened insert in Figure 2. For this image, the BioTRIFT ion optics were optimized for features at a height of 0 μm (i.e., the ITO slide), which means that the total effective focal depth and high sensitivity region of the FMM system may extend below the "0 μm" point.

Although sensitivity and image focus were not observably altered between 0 and 218 μm, the location of the primary ion beam (and thus of the ejected ion images) changes depending on surface height. This surface-height shift may be easily corrected by adjusting the primary ion beam deflection optics to keep the beam centered. However, if these adjustments are not performed, the edges of the ion images will drift outside the field of view of the detector, leading to lower signal intensity in these areas. **Figure S3** demonstrates this effect when the stack of five TEM grids shown in Figure 2 is imaged and no beam position adjustments are performed.
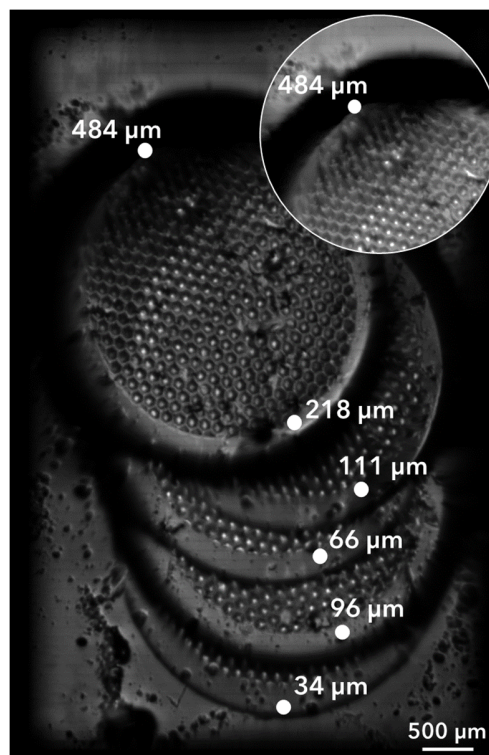
Figure 2. FMM TIC image of five TEM grids stacked on top of each other, showing the height tolerance of the method to be at least 218 μm. Digitally brightened zoom-in of the highest point of the bent grid is included in the top-right corner. The height of points on each TEM grid was determined by SEM analysis.

Improved speed of imaging of a large area

A composed surface containing a 50 μm thick sectioned lemon slice combined with other elements with unique chemical and spatial features was prepared to test the practicality of the improved speed enabled by the encoders and the ability of FMM to image large-area biological tissues. An area of 42.5×26 mm was imaged with a measurement time of 264.6 s which is a rate of 4.18 mm^2 s^{-1} (**Figure 3a**). This imaging rate is approximately 8.5 times faster than the previously reported 0.49 mm^2 s^{-1}.[21] At a pixel size of 1 μm, this image is >1.1 billion pixels and the pixel acquisition rate is 4.176 million pixels s^{-1}. For reference, currently fast microprobe-mode MSI is generally restricted to imaging below 1 000 pixels s^{-1}.[30–32] Even assuming a single TOF cycle per mass spectrum, for a hypothetical instrument if each TOF cycle requires 100 μs, microprobe mode is mathematically incapable of imaging faster than 10 000 pixels s^{-1}. Although 4.176 million pixels s^{-1} was demonstrated here, it is likely that improvements in ion image field of view and instrument optimization could increase FMM to be well over 10 million pixels s^{-1}. Optimizable parameters that may improve FMM speed are increases in motor speed, higher voltage electronics to enable shorter TOF cycles, and corresponding improvements in detector technology such as the Timepix4.[33]
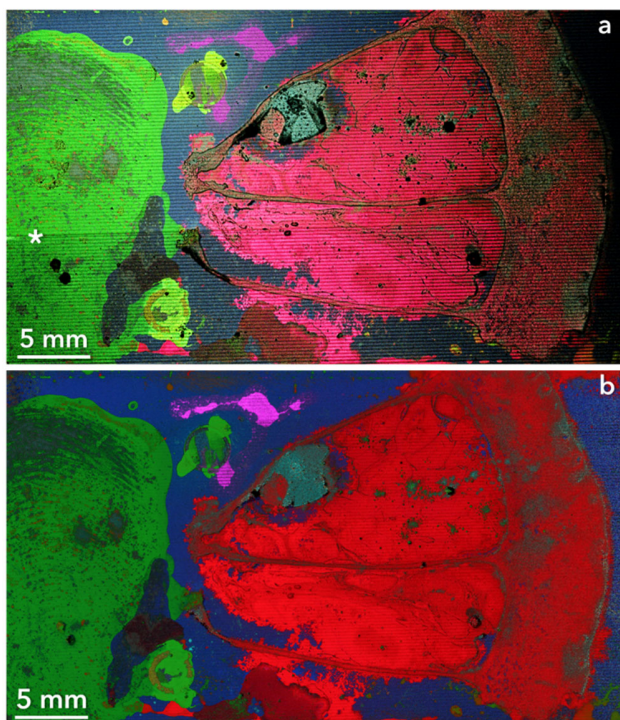
Figure 3. Mass colored FMM images of a 42.5 × 26 mm² of the "composed surface" including Na$^+$ (green, present primarily in the fingerprint), HoO$^+$ (magenta, present above and around the top TEM grid), In$^+$ (blue, present as a background), Cu$^+$ (yellow, present in the lower TEM grid), K$^+$ (red, in the lemon section), and m/z 57, an organic fragment (cyan, present in the lemon section's seed). (**a**) A single-pass ion image that was acquired at 4.18 mm² s^{-1} in under 4.5 min. The asterisk in (**a**) indicates the horizontal row below which the image has been digitally brightened to match the top of the image due to detector instability. (**b**) A multi-pass ion image composed of seven measurements all of the same area as the single-pass image. The total imaging time for all seven passes of the image in (**b**) was 32.75 min., a rate of 0.562 mm² s^{-1}.

The impact of instrumental variations and image artefacts, such as the row pattern observed in Figure 1 and in zoom-ins of Figure 3 (**Figure S4**), can be decreased by addition of multiple passes of the same area. These multi-pass acquisitions are feasible because of the exact coordinates provided by the encoders. Seven measurements of the composed surface sample were collected in 1964.9 s (32.75 min) and combined into one image (**Figure 3b**). Comparing this multi-pass image to the single run image in Figure 3a, shows the clear increase in image homogeneity as well as chemical information. The image acquired in Figure 3a darkens perceptibly due to detector instability. The bottom third of Figure 3a has therefore been digitally brightened to more closely match the top of the image and show that mass information is still present despite the change in detector response. This detector instability was present and visible in all seven individual passes acquired for Figure 3b, however the overall construction reduced the visibility of such detector instability effects on the constructed image. Individual features are also, as expected, more visible in the multi-pass image, especially where the total ion count is low in the individual images (Figure S4).

The image acquired in Figure 3a darkens perceptibly due to detector instability. The bottom third of Figure 3a has therefore been digitally brightened to more closely match the top of the image and show that mass information is still present despite the change in detector response. This detector instability was present and visible in all seven individual passes acquired for Figure 3b, however the overall construction reduced the visibility of such detector instability effects on the constructed image.

Multi-pass image homogeneity may be improved further by alternating horizontal and vertical passes, rather than only using horizontal passes.

Multi-pass mode allows pausing or stopping the imaging at any time after the first pass while still resulting in complete coverage of all sample area. Each pass would only improve the number of ions observed, which improves image contrast and chemical information. This "dynamic time mode" is in contrast to the previous mode of FMM imaging where pausing or stopping an experiment would result in an incomplete image. Furthermore, by enabling such quick scans of large areas, regions of interest (ROIs) may be able to be more easily selected and imaged at a slower rate to facilitate higher molecular information.

Conclusion

The addition of exact coordinates for FMM image construction has enabled accurate image construction at higher stage velocity speeds compared to previous work. In principle, even higher speeds may be possible as the analytical speed is only dependent on the electrical, mechanical, and detector-based specifications of the instrument. FMM also displays high tolerance to surface topographical variations of at least 218 μm. This was demonstrated by imaging a 50 μm thick section of lemon within a composed surface sample over a lateral distance of 42.5 mm. This sample was imaged at 4.18 mm² s^{-1} and 4.176 million pixels s^{-1}, which is 8.5× faster than previously reported FMM imaging and ~4,176× faster than the fastest microprobe-mode MSI instruments. Additionally, the use of exact coordinates enables multi-pass FMM images to be acquired as well as a "dynamic time mode" imaging. This dynamic time mode allows stopping an imaging experiment at any point after the first pass is acquired while retaining the image of the total sample area. The application of such a mode may be helpful for time-limited studies, increasing throughput, and help expand the MSI field further.

Associated Content

Supporting Information

Photograph of the added encoders, SEM-micrograph of the stacked grids, FMM-TIC images of the stacked grids showing manual beam steering improvements, zoom-ins and highlighted areas of the single-pass and multi-pass composed surface sample mass images.

Author Information

Corresponding Author

* Ian G. M. Anthony – The Maastricht MultiModal Molecular Imaging Institute (M4i), Division of Imaging Mass Spectrometry, Maastricht University, 6229 ER, Maastricht, The Netherlands; orcid.org/0000-0003-0433-8343; Email: i.anthony@maastrichtuniversity.nl

Author Contributions

E.S., P.H., F.G., and I.G.M.A. added the encoders to the FMM instrument. E.S. conceived the experiments and carried out all measurements. I.G.M.A. altered FMM image construction and instrument control software to enable the encoder-based improvements. R.M.A.H., S.V.N., and I.G.M.A. secured funding. E.S. wrote the final manuscript with input from I.G.M.A. All authors have given approval to the final version of the manuscript.

Notes

The authors declare no competing financial interest.

Acknowledgement

References

1 A. R. Buchberger, K. DeLaney, J. Johnson and L. Li, *Anal. Chem.*, 2018, **90**, 240–265.

2 X. Guo, X. Wang, C. Tian, J. Dai, Z. Zhao and Y. Duan, *Talanta*, 2023, **264**, 124721.

3 V. Wu, J. Tillner, E. Jones, J. S. McKenzie, D. Gurung, A. Mroz, L. Poynter, D. Simon, C. Grau, X. Altafaj, M.-E. Dumas, I. Gilmore, J. Bunch and Z. Takats, *Anal. Chem.*, 2022, **94**, 10035–10044.

4 I. S. Gilmore, S. Heiles and C. L. Pieterse, *Annu. Rev. Anal. Chem.*, 2019, **12**, 201–224.

5 V. Pareek, H. Tian, N. Winograd and S. J. Benkovic, *Science*, 2020, **368**, 283–290.

6 P. Hinners and Y. J. Lee, *J. Mass Spectrom.*, 2020, **55**, e4631.

7 A. Skriba and V. Havlicek, *Eur. J. Mass Spectrom.*, 2018, **24**, 124–128.

8 M. Senoner and W. E. S. Unger, *J. Anal. At. Spectrom.*, 2012, **27**, 1050–1068.

9 A. Alvarez-Martin, J. Quanico, T. Scovacricchi, E. Avranovich Clerici, G. Baggerman and K. Janssens, *Anal. Chem.*, 2023, **95**, 18215–18223.

10 Y. Liu, X. Ma, Z. Lin, M. He, G. Han, C. Yang, Z. Xing, S. Zhang and X. Zhang, *Angew. Chem. Int. Ed.*, 2010, **49**, 4435–4437.

11 C. Bouvier, A. Brunelle and S. Van Nuffel, in *Applications of Mass Spectrometry for the Provision of Forensic Intelligence*, eds. S. Francese and S. Bleay, Royal Society of Chemistry, 2023, pp. 236–264.

12 B. M. Prentice, *J. Mass Spectrom.*, 2024, **59**, e5016.

13 L. A. McDonnell and R. M. A. Heeren, *Mass Spectrom. Rev.*, 2007, **26**, 606–643.

14 M. F. Wang, A. N. Joignant, A. L. Sohn, K. P. Garrard and D. C. Muddiman, *J. Mass Spectrom.*, 2023, **58**, e4911.

15 R. Castaing and G. Slodzian, *J. Mass Spectrom.*, 2021, **56**, e4800.

16 J. H. Jungmann, L. MacAleese, J. Visser, M. J. J. Vrakking and R. M. A. Heeren, *Anal. Chem.*, 2011, **83**, 7888–7894.

17 A. Kiss, J. H. Jungmann, D. F. Smith and R. M. A. Heeren, *Rev. Sci. Instrum.*, 2013, **84**, 013704.

18 F. M. Green, M. E. Castellani, Y. Jia, A. Eyres, N. Smith, S. Thompson, P. Blenkinsopp, M. Burt, C. Vallance, J. Bunch, Z. Takats and M. Brouard, *J. Am. Soc. Mass Spectrom.*, 2023, **34**, 1272–1282.

19 J. H. Jungmann, L. MacAleese, R. Buijs, F. Giskes, A. De Snaijer, J. Visser, J. Visschers, M. J. J. Vrakking and R. M. A. Heeren, *J. Am. Soc. Mass Spectrom.*, 2010, **21**, 2023–2030.

20 J. H. Jungmann, D. F. Smith, L. MacAleese, I. Klinkert, J. Visser and R. M. A. Heeren, *J. Am. Soc. Mass Spectrom.*, 2012, **23**, 1679–1688.

21 A. Körber, J. D. Keelor, B. S. R. Claes, R. M. A. Heeren and I. G. M. Anthony, *Anal. Chem.*, 2022, **94**, 14652–14658.

22 W. Gao, S. W. Kim, H. Bosse, H. Haitjema, Y. L. Chen, X. D. Lu, W. Knapp, A. Weckenmann, W. T. Estler and H. Kunzmann, *CIRP Ann.*, 2015, **64**, 773–796.

23 L. A. McDonnell, T. H. Mize, S. L. Luxembourg, S. Koster, G. B. Eijkel, E. Verpoorte, N. F. de Rooij and R. M. A. Heeren, *Anal. Chem.*, 2003, **75**, 4373–4381.

24 A. McCann, S. Rappe, R. La Rocca, M. Tiquet, L. Quinton, G. Eppe, J. Far, E. De Pauw and C. Kune, *Anal. Bioanal. Chem.*, 2021, **413**, 2831–2844.

25 Y. Vercammen, N. Moons, S. Van Nuffel, L. Beenaerts and L. Van Vaeck, *Appl. Surf. Sci.*, 2013, **284**, 354–365.

26 B. Bartels, P. Kulkarni, N. Danz, S. Böcker, H. P. Saluz and A. Svatoš, *RSC Adv.*, 2017, **7**, 9045–9050.

27 M. Kompauer, S. Heiles and B. Spengler, *Nat. Methods*, 2017, **14**, 1156–1158.

28 D. Dreisbach, G. Petschenka, B. Spengler and D. R. Bhandari, *Anal. Bioanal. Chem.*, 2021, **413**, 2125–2134.

29 O. Armbruster, A. Naghilou, H. Pöhl and W. Kautek, *J. Opt.*, 2016, **18**, 095401.

30 L. Keren, M. Bosse, S. Thompson, T. Risom, K. Vijayaragavan, E. McCaffrey, D. Marquez, R. Angoshtari, N. F. Greenwald, H. Fienberg, J. Wang, N. Kambham, D. Kirkwood, G. Nolan, T. J. Montine, S. J. Galli, R. West, S. C. Bendall and M. Angelo, *Sci. Adv.*, 2019, **5**, eaax5851.

31 N. Ogrinc Potočnik, T. Porta, M. Becker, R. M. A. Heeren and S. R. Ellis, *Rapid Commun. Mass Spectrom.*, 2015, **29**, 2195–2203.

32 M. Le Rochais, P. Hemon, J.-O. Pers and A. Uguen, *Front. Immunol.*, , DOI:10.3389/fimmu.2022.859414.

33 X. Llopart, J. Alozy, R. Ballabriga, M. Campbell, R. Casanova, V. Gromov, E. H. M. Heijne, T. Poikela, E. Santin, V. Sriskaran, L. Tlustos and A. Vitkovskiy, *J. Instrum.*, 2022, **17**, C01044.